Theoretical predictions of disclination loop growth for nematic liquid crystals under capillary confinement

Alireza Shams, Xuxia Yao, Jung Ok Park, Mohan Srinivasarao, and Alejandro D. Rey

Phys. Rev. E **90**, 042501 — Published 14 October 2014

DOI: 10.1103/PhysRevE.90.042501

Theoretical Predictions of Disclination Loop Growth for Nematic Liquid Crystals under Capillary Confinement

Alireza Shams[1], Xuxia Yao[2], Jung Ok Park[2,3], Mohan Srinivasarao[2,3,4] and Alejandro D. Rey[1]*

[1]Department of Chemical Engineering, McGill University, Montreal, Quebec H3A 0C5, Canada

[2]School of Materials Science and Engineering, Georgia Institute of Technology, Atlanta, GA 30332, USA

[3]Center for Advanced Research on Optical Microscopy, Georgia Institute of Technology, Atlanta, GA 30332, USA

[4]School of Chemistry and Biochemistry, Georgia Institute of Technology, Atlanta, GA 30332, USA

* Corresponding author: alejandro.rey@mcgill.ca

TABLE OF CONTENTS FIGURE

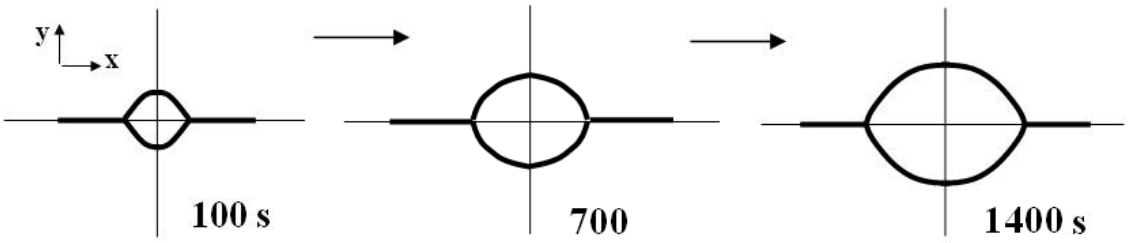

Keywords: +1/2 disclination loops, capillary confinement, line tension, bending tension.

Abstract

The combination of low elasticity modulus, anisotropy, and responsiveness to external fields drives the rich variety of experimentally observed pattern formation in nematic liquid crystals under capillary confinement. External fields of interest in technology and fundamental physics are flow fields, electro-magnetic fields, and surface fields due to confinement. In this work we present theoretical and simulation studies of pattern formation of nematic liquid crystals disclination loops under capillary confinement including a branching processes from m=+1 disclination line to two m=+1/2 disclination curves that describes the post nucleation and growth regime of the textural transformation from radial to planar polar textures. The early post-nucleation and growth of emerging disclination loops in cylindrical capillaries is characterized using analytical and computational methods based on the nematic elastica that takes into account line tension and line bending stiffness. Using sub diffusive growth and constant loop anisotropy, we find that the solution to the nematic elastica is a cusped elliptical geometry characterized by exponential curvature variations. The scaling laws that govern the loop growth reflect the tension/bending elasticity balance and reveal that the loop dilation rate depends on the curvature and normal velocity of the disclination. The line energy growth is accommodated by the decrease in branch point curvature. These finding contribute to the evolving understanding of textural transformations in nematic liquid crystals under confinement using the nematic elastic methodology.

Keywords: *Liquid crystals, Modeling, Disclination, Defect dynamics, kinematic, viscoelastic property*

1. Introduction

Nematic liquid crystals are anisotropic viscoelastic materials that exhibit the anisotropy of crystals and the fluidity of viscous liquids; their macroscopic orientation is characterized by the unit director vector **n**. Phase transitions, external electromagnetic fields, shear flows, and confinement usually generate singular and non-singular orientational defects [1-13]. Disclination formation in nematic liquid crystals under confinement is a subject of continuing interest since frustration emanating from fixed orientation at curved bounding surfaces is common in applications [13-18]. Defects in nematic liquid crystals include disclinations lines, walls and point defects [1, 19]. A disclination line is characterized by a quantized charge m which specifies the amount of rotation when encircling the line and the sign (+/-) associated with the charge denotes the sense of rotation [2]. Since the energy per unit length or line tension associated with a line defect scales with m^2, ±½ lines are energetically preferred [2, 9]. The defect ring has been investigated previously by Luca and Rey [20], here we focus on the bending effect on the dynamics and kinematics of the radial disclination loops growth. Straight disclinations only store line tension energy since the planes of director gradients are parallel. On the other hand the energy of a planar curved disclination line contains both tension and bending contributions since the planes of director gradients are splayed [7]. In the most general case of spiral disclinations, additional torsion elasticity arises. This paper considers curved planar disclination loops under capillary confinement. Figure 1 shows a schematic of a +1/2 disclination loop attached to +1 line segments, relevant to this paper. The splay of the cross sectional planes

as one moves along the line generate line bending stiffness since $\partial \nabla_{\perp}\mathbf{n} / \partial s \neq 0$; where $\nabla_{\perp}\mathbf{n}$ are normal gradients and "s" is the arc-length.

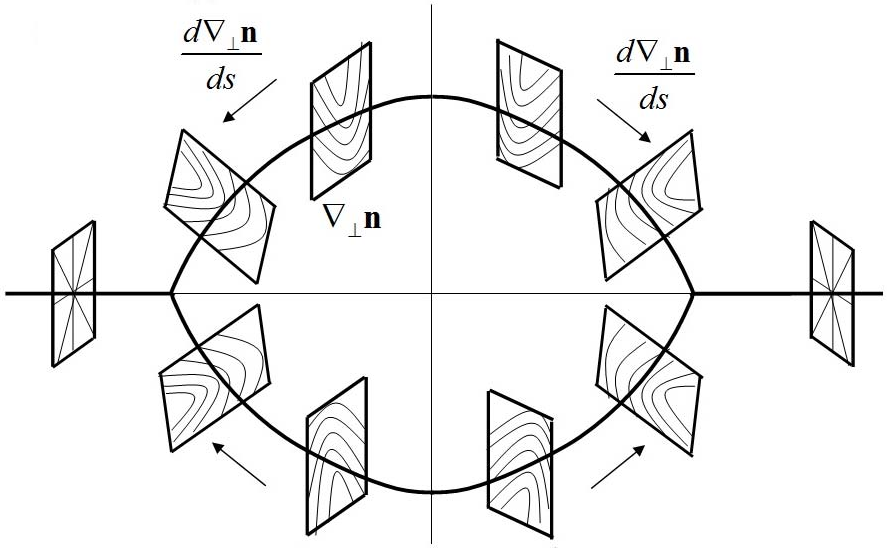

Figure 1. Schematic of a +1/2 disclination loop attached to a +1 line and director field in the cross-sectional plane. Disclination bending stiffness arises when $\partial \nabla_{\perp}\mathbf{n} / \partial s \neq 0$ (adapted from ref. 7)

Texturing of NLCs under cylindrical capillary confinement with homeotropic anchoring is summarized in a generic texture phase diagram [20, 21] shown in Figure 2, which contains four textures: (i) polar radial line defect (PR), (ii) planar polar line defect (PP), (iii) escape radial ring defect (ERRD), and (iv) escape radial (ER) textures. This figure shows the stability range of each texture and provides a wealth of important information on interfacial science, phase transitions, elasticity, and defect physics. For example, the PR/PP boundary describes the defect instability: $m = +1 \rightarrow 2 (m = +1/2)$, emanating from the branch point to form a loop, driven by bulk elasticity reduction, and hence its location on the texture diagram provides information on bulk elasticity.

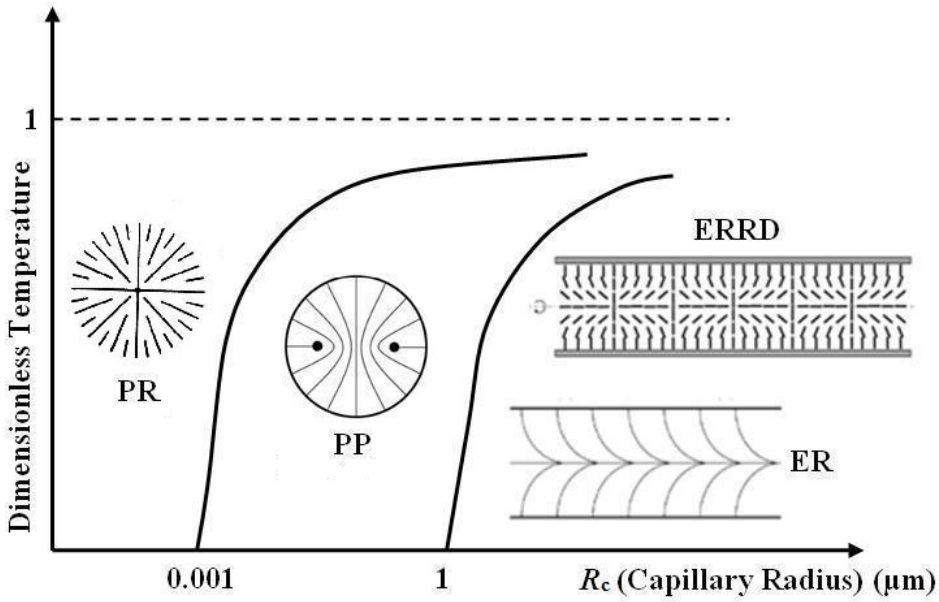

Figure 2. Texture phase diagram in terms of dimensionless temperature (T/T_{NI}) as a function of the capillary radius for uniaxial nematics under capillary confinement, indicating the geometric and thermal conditions. The horizontal dashed line is the nematic/isotropic transition temperature T_{NI}. PR is the planar radial line defect texture with a m=+1 defect at the center, PP is the planar polar line defect texture with two m=+½ defects, ER is the escaped radial texture where the director tilts out of the cross sectional plane, and ERRD is the escaped radial ring defect texture, consisting of a periodic lattice of alternating +1 and -1 point defects separated by a distance close to the capillary radius. (Adapted from reference 21).

The nature of the PR→PP transition in principle can be spinodal (SD) or nucleation and growth (NG), but elastic energy estimates show that NG will prevail. In the SD mode the entire +1 line splits into two +1/2 lines along the entire capillary of length L that separate under charge repulsion. On the other hand in the NG mode, a number 'n' of +1/2 loops nucleate and grow along the initial +1 line. Since the elastic length scale associated with the director **n** is the capillary radius R_c, the distance between the nucleating loops is of the order of R_c=L/n. If the energy cost (creating two cores and two interfaces) of splitting a +1 line of length L is L_E in the SD mode then energy of nucleating n loops in the NG mode is $L_E\left(R_{loop}/R_c\right) < L_E$. Figure 3 shows a schematic of the NG mode of the PR→ PP transition consisting of:

(i) initial stage: nucleation on a pre-existing +1 line of "n" +1/2 loops separated by a distance of the order of R_c=L/n (Figure 3(a));

(ii) early stage: vertical and horizontal growth of +1/2 loops, involving the motion of branch points (BP) that join the +1/2 loops and the +1 line segments with a constant branch angle (see Figures 3(b) and 4);

(iii) intermediate stage: coarsening and horizontal growth saturation of the +1/2 loops, where the vertical saturation is $2y_\infty = 1.33R_c$ (Figure 3(c)).

(iv) late stage: formation of the PP texture with two parallel +1/2 lines separated by a distance $2y_\infty = 1.33R_c$ (Figure 3(d)).

We emphasize that this paper deals with a single loop growth and that issues with multiple loops, loop-loop interactions and the exact loop-loop nulceation distance are not considered.

In this paper we only consider the early stage (ii). Stages (iii) and (iv) were discussed in [7-9,22] where it is shown that the bending to tension ratio is a function of the capillary geometry. *The key issue of interest in the present paper is: what is the evolving shape of the +1/2 disclination loop that reflects the impact of line tension and bending stiffness of disclination lines under given growth kinetics?* In the present problem each of the +1/2 disclination loops is attached to a +1 string and they grow driven by the texture transformation process. The related phenomenon of growth of isolated disclination loops in a cylindrical capillary was previously discussed by de Luca and Rey [20].

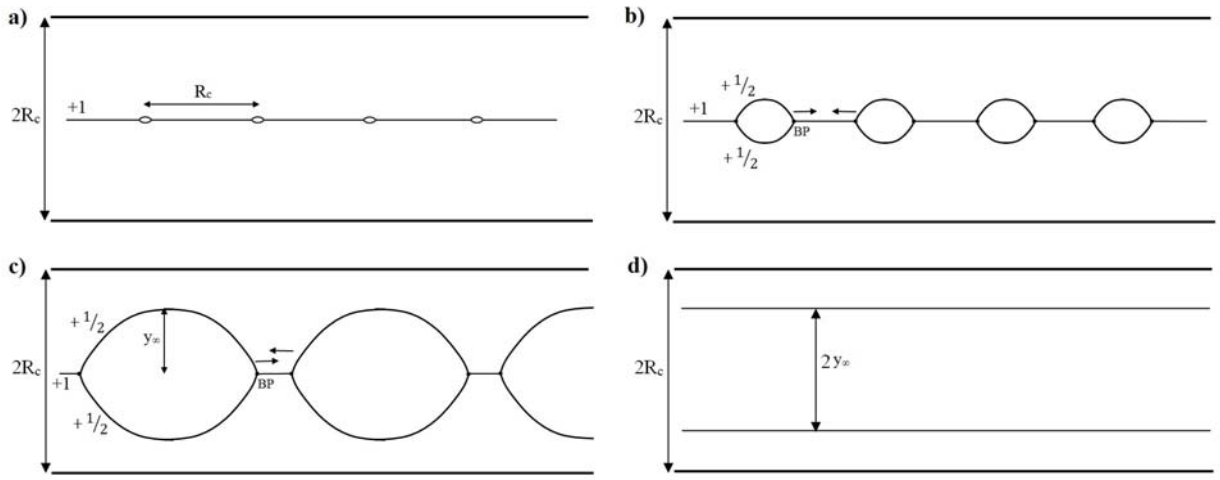

Figure 3. The nucleation and growth process of domains consisting of +1/2 loops that eventually lead to sections with well-formed PP textures; **(a)** Initial nucleation stage, defect points appear on the +1 disclination line. The distance between two points is of the order of the capillary radius (R_c); **(b)** early growth stage including textural transitions from high order +1 disclination into energetically less costly +½ disclinations. The energy difference between the two textures, which generates the constant motion of the branch point (BP); **(c)** Intermediate coarsening stage. The loop expansion stops when the loop vertical radius reaches the final defect distance, y_∞, but BPs still moves horizontally; **(d)** Final stage. After collision of branch points, we see the relaxation of the line shape leading to 2 +1/2 disclination lines separated by distance y_∞.

The organization of this paper is as follows. Section 2 presents the theoretical framework and equations for disclination loop shape and kinematics. Section 3 presents the results including disclination curvature and space curve as a function of arc-length, the effect of time on the disclination shape and energy, the relations between loop geometry and disclination elasticity and the kinematics of the disclination loop. Section 4 presents the conclusions. The details of computational method are provided in Appendix I. Appendix II discusses the branch angle shown in figure 4 and establishes the relation between material length scale, l_M, and geometric length scale that is behind a fixed branch angle value of 60^o and Appendix III compares the

viscous and tension elasticity terms presented in the shape equation. As noted above this paper builds on our previous work on nematic liquid crystals under capillary confinement [7-9].

2. Disclination Loop Shape Model and Simulation

2.1. Disclination Loop Geometry

Figure 4 shows the (x,y) coordinate system and geometry of a +1/2 disclination loop consisting of two planar m=+1/2 disclination lines emanating from two branch points located at $(x,y)=\left(\pm x_b(t),0\right)$. The semi-axes $\left(R_x(t),R_y(t)\right)$ grow in time as dictated by the driving energy minimization.

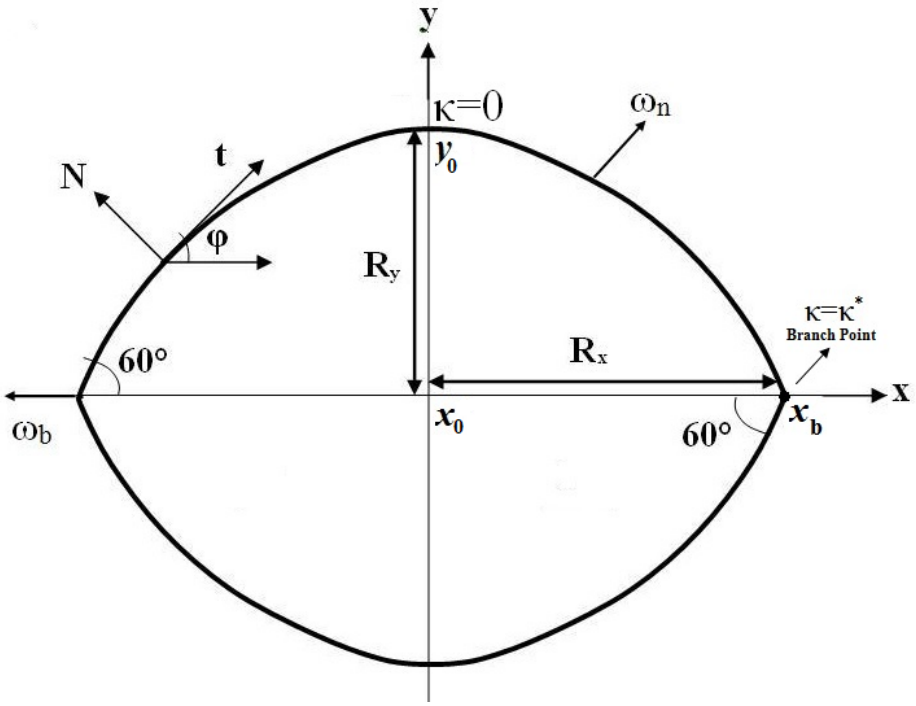

Figure 4. Schematic of the coordinate system and geometry of two m=+ ½ lines emanating from the branch point at $x=x_b$, y=0. The x-axis is along the capillary axis. The angle between the x-axis and the tangent vector **t** is φ, **N** is the unit normal, and s the arc-length. The branch point angle, φ_o, is 60°. R_x is the loop long radius which is the half distance between two branch points and R_y is the loop short radius which is the half-separation distance between the two + ½ lines. ω_n is the normal velocity of the loop growth, ω_t is the tangent velocity and ω_b is the branch point velocity

respectively. At the top and the bottom of the loop, $(x_0,\pm y_0)$, $\kappa=0$ and at the branch point, $(\pm x_b,0)$, $\kappa=\kappa^*$.

The unit tangent **t** and the unit normal **N** to the filament are given by [7-9]:

$$\mathbf{t}(s,t)=\frac{\partial \mathbf{r}(s,t)}{\partial s} \quad ; \quad \frac{\partial \mathbf{t}(s,t)}{\partial s}\equiv\frac{\partial^2 \mathbf{r}(s,t)}{\partial s^2}=\kappa\,\mathbf{N}(s,t) \tag{1a,b}$$

where $\boldsymbol{\kappa}=\partial\mathbf{t}/\partial s$ is the curvature, **r** is the position vector and s the arc length, respectively. **t** is a unit vector which is expressed with the tangent angle φ(s): $\mathbf{t}(s)=(\cos\varphi(s),-\sin\varphi(s))$. In the normal angle parameterization, the curvature is: $\kappa=\partial\varphi/\partial s\equiv\varphi_s$. According to Figure 4, to describe the disclination as an evolving space curve $y(x,t)$, we need to specify: (i) the loop curvature κ(s), (ii) the tangent angle at the branch point φ_o, and (iii) the loop amplitude R_y (t), and (iv) the location of the branch point $R_x(t)$.

2.1. Disclination Shape Equation

In this section we derive the disclination shape equation by formulating the force balance equation on the line due to internal and external stresses. Internal stresses include line tension and line bending forces whose expressions are derived using Frank elasticity. The shape equation of the +1/2 disclination is then used to formulate the shape equation for the growing +1/2 loop.

(a) Disclination line tension and bending stiffness

The Frank gradient elasticity density *f* for uniaxial NLCs, using the one constant approximation is [2]:

$$f = \frac{K}{2}\left((\nabla \cdot \mathbf{n})^2 + (\nabla \times \mathbf{n})^2\right) \quad (2)$$

Minimizing the total free energy leads to the Euler-Lagrange equation: $K\nabla^2\mathbf{n} = \lambda\mathbf{n}$; K is the Frank elastic constant, and λ is the Lagrange multiplier that takes into account the unit length restriction $\mathbf{n}\cdot\mathbf{n} = 1$. The +1/2 axial disclination that forms the loop is characterized by a planar director field perpendicular to the direction of the line $\mathbf{n} = (\cos\psi, \sin\psi, 0)$. In planar polar coordinates (r,φ), a wedge disclination solution to the Euler Lagrange equation is $\psi = m\varphi + C$, where the defect charge m is a multiple of $\pm 1/2$ and C a constant. The occurrence of half-integer winding numbers is a result of the nematic symmetry and physical identity of the alignment **n** and –**n** [22]. By integrating eqn. (2) in a cylinder of radius R_c, one obtains the line tension $\gamma_o(PP)$ of a single straight m=+1/2 disclination in the PP texture[21]:

$$\gamma_{1/2} = \gamma_o(PP) = \underbrace{\frac{\pi K}{2}\left(\ln\left(\frac{R_c^2}{2r_c y_\infty}\right)\right)}_{\gamma_{o,1/2}} + \pi\sigma_c r_c^2 \quad (3)$$

where R_c is the capillary radius, r_c is the core radius, σ_c is the core energy density that is usually assumed to be negligible in comparison to the other terms and $2R_y$ is the distance between the two +1/2 lines defined in Figure 4. The total line energy $\gamma_{1/2}$ (energy/length) of a curved +1/2 disclination is given by the sum of the core energy $\pi\sigma_c r_c^2$, bare line tension $\gamma_{0,1/2}$, and the bending $k_c\kappa^2/2$ contributions [7]:

$$\gamma_{1/2} = \pi\sigma_c r_c^2 + \gamma_{0,1/2} + \frac{k_c}{2}\kappa^2;\ k_c = \frac{\pi K R_c^2}{\sqrt{2}} \quad (4a,b)$$

where k_c is the bending modulus (energy × length) and only the leading order bending term is retained. Equation (4b) is applicable to the intermediate coarsening stage (see mode (iii)

discussed above and [7]), but in the post nucleation and growth stage studied here we show below (see eqn. (31b)) that it is a function of R_y. To find the disclination shape equation, we perform the following stress balance.

(b) Disclination shape equation

The force balance equation is written by the sum of line force $\nabla_\ell \cdot \mathbf{T}$ and the surrounding medium force [23]:

$$\nabla_\ell \cdot \mathbf{T} + \oint_{\partial F} \left(\mathbf{N} \cdot \mathbf{T}_b \right) d\ell = \gamma_1 \boldsymbol{\omega} \tag{5}$$

where $\mathbf{T}$ is the + ½ disclination line elastic stress tensor, $\nabla_\ell (\bullet) = \mathbf{t}\, \partial(\bullet)/\partial s$ is the line gradient operator, $\mathbf{N}$ is the unit normal vector and $\mathbf{T}_b$ is the bulk stress tensor, $\mathbf{N} \cdot \mathbf{T}_b$ is the elastic force acting on the disclination by the bulk, and the integral is over the disclination circumference ∂F, γ_1 is the rotational viscosity, and ω the velocity of the line. To find the m=+1/2 line elastic stress tensor $\mathbf{T}$, we perform a variation of the total line elastic free energy due to tangential and normal displacements and find [23, 24]:

$$\mathbf{T} = \left(\gamma_{1/2} - \mathbf{M} : \mathbf{b} \right) \mathbf{I}_\ell - \frac{\partial M}{\partial s} \mathbf{t}\mathbf{N} \tag{6}$$

where $\gamma_{1/2} \mathbf{I}_\ell$ is the thermodynamic tension stress analogous to 3D pressure. The elastic line stress $\mathbf{T}$ has a mechanical contributions ($-\mathbf{M} : \mathbf{b}$), since there can be no bending without tension; here $\mathbf{b}$ is the line curvature tensor given by $\mathbf{b} = \kappa \mathbf{I}_\ell$. The last term in equation (6) are the bending stresses that arise under curvature gradients ($\partial \kappa / \partial s \neq 0$). The scalar moment M, line moment tensor $\mathbf{M}$, and line elastic stress tensor $\mathbf{T}$ are:

$$M = k_c \kappa, \ \mathbf{M} = k_c \kappa \mathbf{I}_\ell \ ; \ \mathbf{T}^e = \left(\gamma_{o,1/2} - \frac{k_c}{2} \kappa^2 \right) \mathbf{I}_\ell - k_c \frac{\partial \kappa}{\partial s} \mathbf{t}\mathbf{N} \tag{7a,b,c}$$

Assuming that bulk dissipation is generated by bulk forces: $\oint_{\partial F}\left(\mathbf{N}\cdot\mathbf{T}_b\right)\mathrm{d}\ell=\gamma_1\boldsymbol{\omega}$, and replacing eqns.(4 and 7) into (6) we find the disclination shape equation , known as *nematic elastica*, as a balance between tension and bending forces:

$$\underbrace{\gamma_{0,1/2}\kappa}_{\text{tension}}-\underbrace{k_c\left(\kappa_{ss}+\frac{\kappa^3}{2}\right)}_{\text{bending}}=0 \tag{8}$$

The diffusive term $k_c\kappa_{ss}=k_c\partial^2\kappa/\partial s^2$ and the nonlinearity $k_c\kappa^3/2$ arise due to the bending stresses in eqn. (5). We assume that $\gamma_{0,1/2}+\mu\partial\kappa/\partial t\approx\gamma_{0,1/2}$ and the line viscosity term is negligible (see Appendix III). Eqn. (8) is a steady nonlinear reaction-diffusion equation, in which the time dependency of the curvature $\kappa(s)$ that describes loop growth enters through transient boundary conditions at the moving branch point $(x_b(t),0)$ and at the $(0,R_y(t))$.

Disclination loop shape equation

For simplicity we use one loop quadrant. For the selected fixed (x,y) coordinates, the amplitude of the loop corresponds to zero arch-length (s=0) , while the branch-point to S*(t). To derive the loop shape equation we subject eqn. (8) to time dependent curvature boundary conditions:

$$s=S^*(t),\ \kappa=\kappa^*(t)=d\phi/ds\big|_{S^*(t)}\ ;\ s=0,\kappa=0 \tag{9a,b,c}$$

where S^* and κ^* are functions of time . The two important parameters in eqns. (8 and 9) that will affect the shape of the loop are the ratio of the tension to bending stiffness $\left(a=\gamma/k_c[=]\text{length}^{-2}\right)$ and the branch point curvature (κ^*) which are functions of capillary size [7].

(d) Disclination space loop

In the selected quadrant the space loop is given by the evolving space curve ((x(t),y(t)). From the Fresnel integrals [25] we have:

$$x\left(s,a,\kappa^{*},t\right)=\int_{0}^{S^{*}(t)}\cos\left(\int_{0}^{s'}\kappa\left(s'',a,\kappa^{*}\right)ds''\right)ds' \tag{10}$$

$$y\left(s,a,\kappa^{*},t\right)=\int_{0}^{S^{*}(t)}\sin\left(\int_{0}^{s'}\kappa\left(s'',a,\kappa^{*}\right)ds''\right)ds' \tag{11}$$

where a is the tension to bending ratio: $\gamma_{0,1/2}/k_c$. The boundary conditions written in terms of *y* and *x* are:

$$x=0,\ y=y_0(t)$$
$$x=x_b(t),\ \left.dy\middle/dx\right|_{x_b}=\tan(60^{\circ}) \tag{12a,b,c}$$

where $x_b(t)$ is the branch point position on the x axis and $y_0(t)= R_y$ is the loop height. Corresponding boundary conditions can be defined for the other loop quadrants. Equation (12) assumes a constant branch angle $\theta_b = 60^{\circ}$, extensively discussed previously [7].

The equations (8, 10-12) are solved simultaneously in the domain $x_{b-}(t)\le x\le x_{b+}(t)$.

(e)Loop growth laws

The time dependent boundary conditions (eq. 12) require loop growth expressions. Growth laws of +1/2 loop growth attached to +1 disclinations under confinement have not been established. Nevertheless using +1 disclination splitting into two +1/2 lines under capillary confinement (SD mode) it was found [21] that in the intermediate stage of the PR → PP transition the defect-defect distance ℓ_{defect} is described by a power law of the type:

$$\ell_{defect}=At^{n} \tag{13}$$

where $n\approx 0.2$. Assuming an anisotropic rate of expansions for the loop, the previous scaling yields:

$$R_x(t) = A_x t^{0.2}$$
$$R_y(t) = A_y t^{0.2} \quad \text{(14a, b)}$$

and the anisotropy ε of the loop is a constant:

$$\varepsilon = \frac{R_y(t)}{R_x(t)} = \frac{A_y}{A_x} \quad (15)$$

In this paper we use as characteristic values A_x=22.5, A_y=15, so the ratio ε= 0.667 is close to what has been observed experimentally [8].

2.2. Kinematic Characterization

During loop growth the normal velocity $\omega_n(s,t)$ is function of arc-length and time (see Figure 5(a) below for details). Figure 5(b) shows the normal, axial and vertical velocity at the branch point. At each point of curves, the normal velocity is a vector sum of the axial and vertical velocities. The axial velocity at the branch point is called branch point velocity. Using the previously established [7-9] constant branch angle, the axial and vertical BP velocities are:

$$\begin{cases} \omega_y(t)\big|_{bp} = \omega_n(t)\big|_{bp} .\sin\left(30^\circ\right) \\ \omega_x(t)\big|_{bp} = \omega_n(t)\big|_{bp} .\cos\left(30^\circ\right) \end{cases} \quad \text{(16a,b)}$$

Hence kinematic compatibility leads to:

$$\frac{\omega_y(t)\big|_{bp}}{\omega_x(t)\big|_{bp}} = \tan(30^\circ) \quad (17)$$

In terms of growth velocities we have a slowdown exponents close to -1:

$$\omega_x(t)\big|_{bp} = 0.2A_x t^{-0.8}; \omega_y(t)\big|_{s=0} = 0.2A_y t^{-0.8} \quad (18)$$

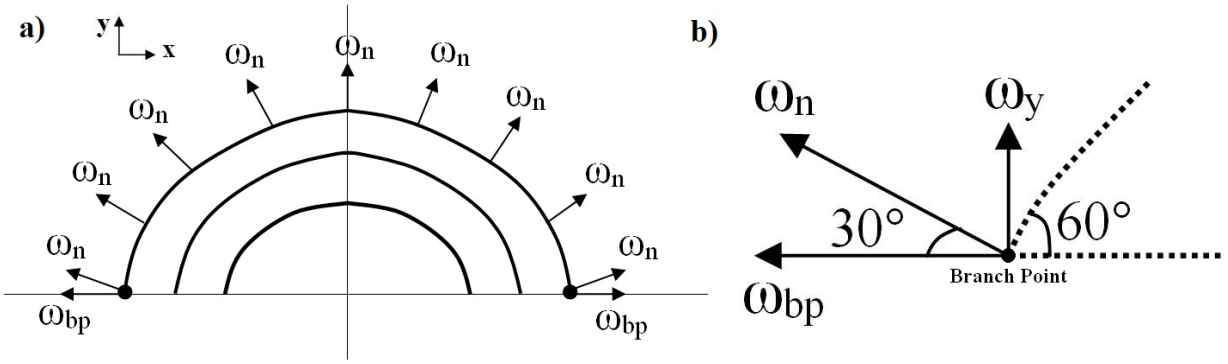

Figure 5. (a) Schematic of the system of parallel curves created as a result of the disclination loops' growth process. The branch point angle remains unchanged during the evolution, so the normal velocity, ω_n, is uniform along the curve; **(b)** The normal velocity at the branch point. The fact of a 60° angle at the branch points leads to a relation between the axial and the vertical velocity (eq. 17) which helps us to predict one from another.

To find the normal velocity $\omega_n(s,t)$ along the disclination curve we can use the transport theorem for a closed loop [23]:

$$\Delta(t) = \frac{dL}{Ldt} = -\frac{1}{L}\int_0^{S^*(t)} \kappa(s,t)\,\omega_n(s,t)\,ds \tag{19}$$

where L(t) is the total length of the disclination curve and $\Delta(t)$ is the dilation of the loop [25,26]. Hence the time-dependent dilation Δ(t) encapsulates the geometry $(\kappa(s,t))$ and kinematics $(\omega_n(s,t))$ of the growing disclination loop.

2.3. Computational Methods

To find the shape of the evolving loop under micron-range confinement we solve equations (8, 10 and 11), subjected to boundary conditions (eq. 12) using a standard iterative methods; see Appendix I. The analytical solution of eq. (8) presented in [7] is used to estimate to initial values for arc-length. The initial time is to=100 s, when the loop shape is a quartic

$y = \pm\left(-9\times10^{-7}x^4 - 0.0065x^2 + 37.17\right)$; all distances used in this paper are in microns. The time step to describe growth is 10 s and the final time is 1400 s, when R_y becomes close to the saturation value $0.665R_c$ [7]. The capillary radius is R_c=100 μm and the branch point angle is fixed at 60° for all cases (see Appendix II).

3. Results and Discussion

We recall that starred values refer to values at the branch points. Unless explicitly mentioned, due to the symmetries of the loop and for brevity we mainly show results for one quadrant.

3.1. Curvature κ(s)

The evolutions of the +1/2 disclination loop is characterized in terms of: (a) the curvature κ(s), (b) the total arc-length S*(t), and the branch-point curvature κ^* (t), and (c) the total loop curvature κ_t (t);

(a) Curvature κ(s). Figure 6(a) shows the curvature κ(s) as a function of arc-length for t=100, 700 and 1400 s for $0<x<x_b$, and fourth quadrant of the disclination curve. The curvature increases exponentially as the branch point is reached and loop expansion decrease κ^* (see also Fig. 6(b)). Complex spatio-temporal changes in the curvature reflect the tension-bending elasticity under growth conditions. Figures 6(b) shows the exponential-like decay of the diffusion-to-nonlinear bending ratio $2\kappa_{ss}/\kappa^3$ as a function of arc-length for t=100, 700 and 1400 s. The figure demonstrates that the relative importance of bending stress (diffusion term κ_{ss}) to tension stress (cubic term κ^3) is maximal at x=0 and vanishes at the branch point.

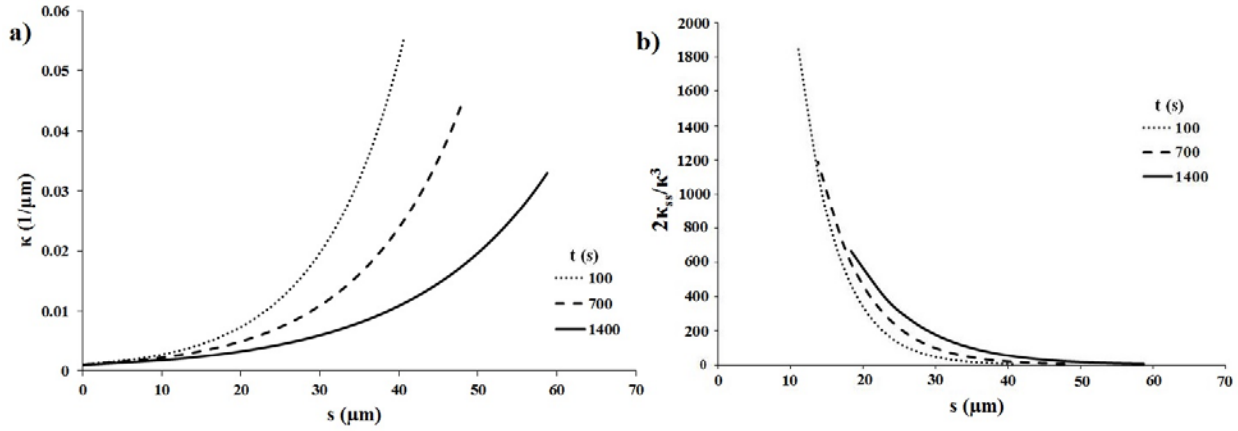

Figure 6. (a) Effect of time on curvature κ(s) as a function of arc-length. For the later time, the final curvature κ^* is smaller; **(b)** The diffusion to nonlinear bending ratio $2\kappa_{ss}/\kappa^3$ as a function of arc-length for *t*=100, 700 and 1400 s. The ratio increases over time.

(b) Total Arc-Length S*(t). Figure 6(a) shows the final arc-length S*(t) as a function of time. The increases from 88.25 μm at *t*=100 s to 134.26 μm at *t*=1400 s is associated with the loop expansion. On the other hand Figure7 (b) shows that as loop grows, the branch point curvature decreases. The data shown in Figs.7 (a-b) can be collapsed into power laws:

$$S^* = 45.3t^{0.15}$$
$$\kappa^* = 0.14t^{-0.19} \qquad (20a,b)$$

Comparing with eqn. (13) we retrieve the expected results: $S^* \approx o\left(R_x + R_y\right); \kappa^* \approx o\left(R_x + R_y\right)^{-1}$, the latter is shown in Figure A2.

The dimensionless number $P = S^*\kappa^*$ which is the ratio of loop growth to maximum loop curvature, shown in Figure 7(c), is a weak function of time as per eqn. (20) and higher than for circular growth ($\left(P \geq \pi R / R = 3.14\right)$.

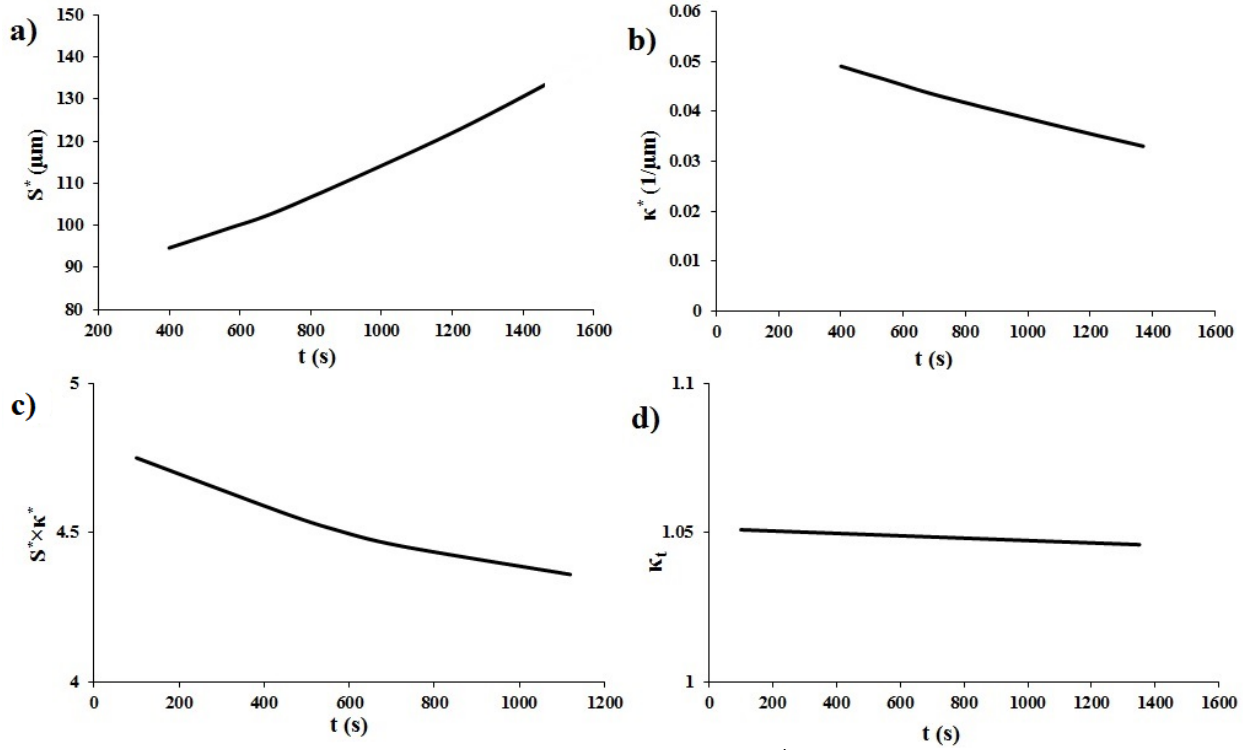

Figure 7. (a) The final arc-length as a function of time. S^* increases by time; **(b)** The branch point curvature as a function of time. κ^* decreases by time; **(c)** The dimensionless number $P = S^*\kappa^*$ as a function of time. This number is larger for smaller loops than for larger loops; **(d)** The total curvature for a quarter loop as a function of time. The total curvature is independent of the time.

(c) *Total Curvature* κ_t. Figure 7(d) shows the total curvature κ_t for a quarter loop as a function of time. The total curvature κ_t is the subtended angle ψ (radians) of the disclination arc (for a circle of radius *R*, the subtended angle is: $\psi = S^*/R$) and is a function of S* as well as κ(s). The subtended angles ψ (radians) is essentially constant because of a constant branch angle [27]:

$$\kappa_t = \int_{\text{Branch Point}}^{\kappa=0 \text{ point}} \frac{\partial \theta}{\partial s}\, ds = \frac{\pi}{2} - \frac{\pi}{6} \tag{21}$$

so the total curvature for all cases should be π/3. The essentially negligible temporal decrease of κ_t shown in Figure 7b is due to unavoidable but negligible computational errors.

3.2. Disclination Curve y(x)

Figure 8(a) shows representative disclination curves $y(x)$, for t=100, 700 and 1400 s. At t=100 s, R_x=52.77 μm and R_y=37.67 μm which increase to R_x=97.22 μm and R_y=65.87 μm at t=1400 s. The disclination curve that satisfies is essentially a quartic

$$y=\pm\left(-\left(\frac{9\times10^{-7}}{t^{0.5}}\right)x^4-\left(\frac{0.0075}{t^{0.03}}\right)x^2+R_y(t)\right) \tag{22}$$

where $R_y(t)=15t^{0.2}$; the quartic fit has a standard deviation of 0.97.

Figure 8(b) shows the changes of the slope of disclination curves over time for $0\le x\le x_{b+}(t)$. The funnel shape reflect the time-invariant fact that the curvature vanishes as we approach x=0.

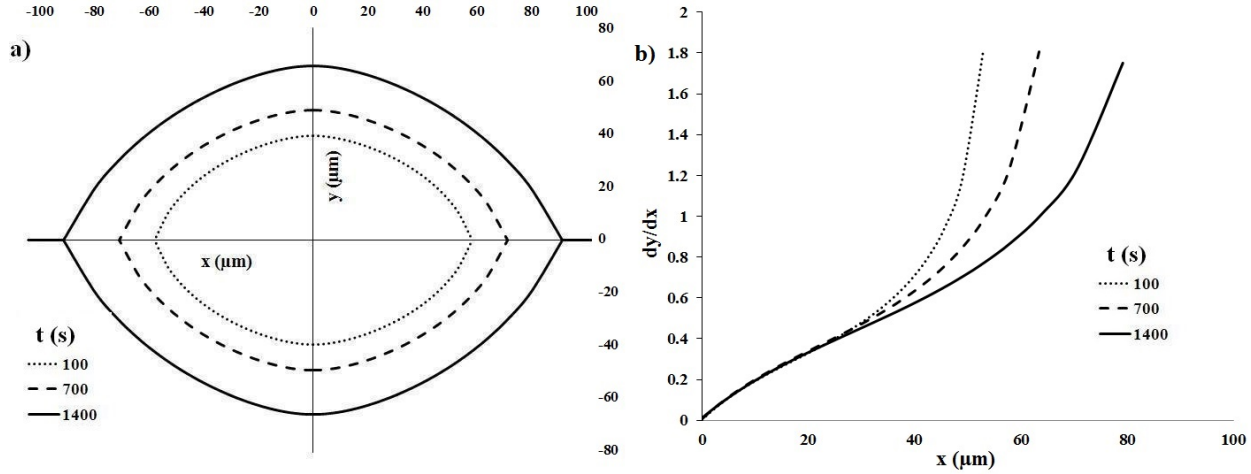

Figure 8. (a) The disclination curves as a function of time. The size of loops increases over time; **(b)** The slope of disclination curves, dy/dx, for t=100, 700 and 1400 s. The rate of changes is faster for the smaller loops.

3.3. Kinematics

Figure 9(a) shows the growth velocities $\left(\omega_x(y=0),\omega_y(x=0),\omega_x(x=x_b)\right)$. These velocities show a power law decrease followed by a terminal velocity. This regime signals proximity to the transition intermediate stage of coarsening characterized by R_y=0.66R_c and

$\omega_x(x = x_{BP}) = \omega_t$, and $\omega_y(x = 0) = 0$, where ω_t is a terminal velocity. At t=1400s, the R_y reaches the saturation value (y_∞=0.66R_c) [7-9] at which the terminal velocity will be around ω_t =0.016 μm/s. This value is rationalized by this fact that the branch points moves slowly which doesn't affect the disclination curve shape. The ordering of the growth velocities follows from kinematic compatibility (eqn. (17)) and growth kinetics (eqn.(18)):

$$\omega_n(t)\big|_{bp} = \frac{\omega_x(t)\big|_{bp}}{\cos\left(30^\circ\right)} > \omega_x(t)\Big|_{bp} = 5.19t^{-0.8} > \omega_y(t)\big|_{s=0} = 3t^{-0.8} \tag{23}$$

Figure 9(b) shows the normal velocity $\omega_n(s,t)$ as a function of arc-length computed from eqns. (18). The time functionally of the normal velocity $\omega_n(s,t)$ is essentially homogeneous over the disclination curve as per eqns. (14), the upper and lower limits decrease as $t^{-0.8}$:

$$\underbrace{\omega_n(s = S^*,t)\big|_{bp} = \frac{5.5}{t^{0.8}}}_{\text{branch point normal velcity}} > \omega_n(s,t) > \underbrace{\omega_n(s = 0,t)\big|_{x=0} = \frac{3}{t^{0.8}}}_{\text{vertical velocityat x=0}} \tag{24}$$

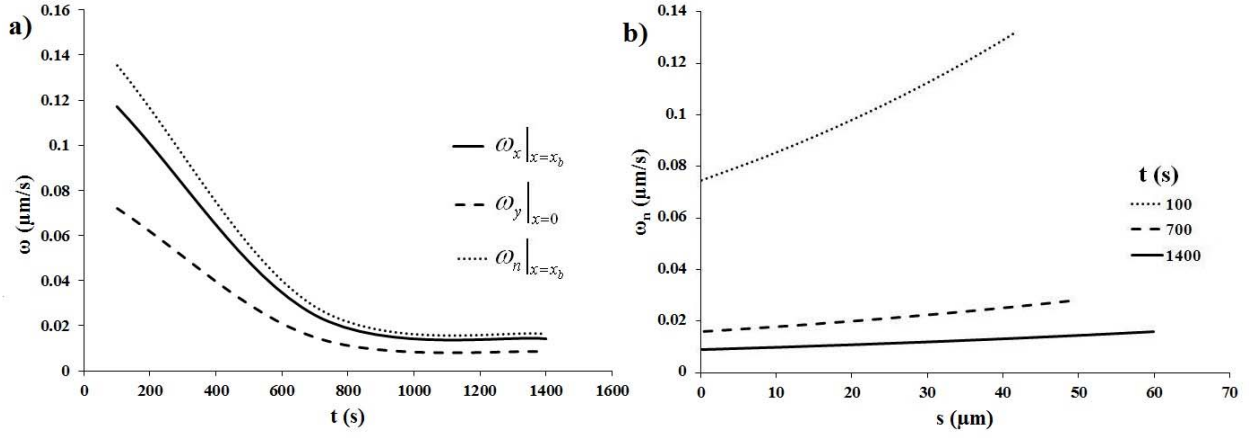

Figure 9. (a) The growth velocity in x and y directions and the normal velocity at the branch point as functions of time. These velocities decrease until they reach a terminal velocity; **(b)** Normal velocity as a function of the arc-length for t=100, 700 and 1400 sec. Over time, the normal velocity becomes a week function of arc-length.

Figure 10(a) shows the loop dilation Δ(t)=(dL/dt)/L as a function of time. The power law for dilation is

$$\Delta = 0.15t^{-1} \tag{25}$$

and follows the growth scaling:

$$\frac{dL}{dt} = 6.8t^{-0.85} \tag{26}$$

Figure 10(b) shows the computed stiffness ratio $a = \gamma_{0,1/2}/k_c$ as a function of R_y. We recall that a (t) $= \gamma_{0,1/2}/k_c$ is not a constant material property but it depends on time, as k_c depends on the confinement (see Fig. A1). The present stiffness ratio data in the nucleation and growth mode can be collapsed into the power law:

$$a(t) = \frac{\gamma_{0,1/2}}{k_c} \equiv \frac{1}{(\ell_M)^2} \approx \frac{4}{R_y^2(t)} \tag{27}$$

where ℓ_M is the material length scale (see also Appendix II). Eqn.(27) simply states that the material length scale ℓ_M is one half of the geometric length scale R_y: $\ell_M = R_y/2$. In the coarsening mode we found [7] that the material length scale is $\ell_M = R_c/3$. Since the limiting value of R_y is: $R_y(t \to \infty) = R_c/3$ we find that long term time limit of eqn.(27) is consistent with our previous result [7] since:

$$\lim_{t\to\infty} R_y \approx \sqrt{\frac{4}{9}} R_c = 0.66 R_c \tag{28}$$

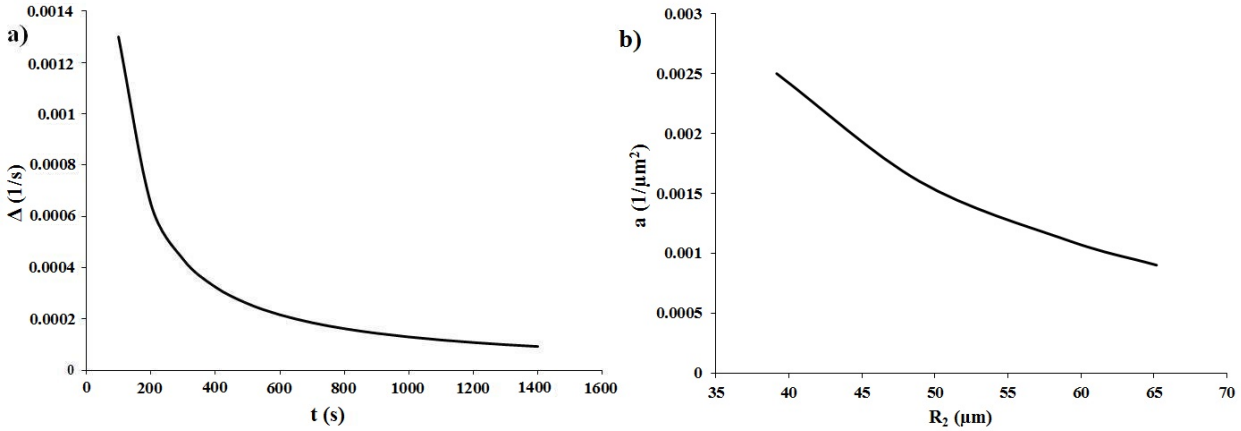

Figure 10. (a) The loop length dilation Δ as a function of time. The loop growth rate decreases as $t^{-0.85}$; **(b)** The stiffness ratio $a(t) = \gamma_{0,1/2} / k$ as a function of the loop short radius R_y. When the loop size increases, $a(t) = \gamma_{0,1/2} / k$ decreases as $4/R_y^2$.

3.4. Disclination Energy

The total energy of a +1/2 disclination loop is the sum of total tension and total bending contributions:

$$E_T = E_b + E_t \tag{29}$$

where E_b and E_t are the total bending and total tension energy defined (for a loop quadrant) by

$$E_t(t) = \int_0^{S^*(t)} \gamma_{o,1/2}(s,t)\, ds; \qquad E_b(t) = \int_0^{S^*(t)} \left(\frac{k_c}{2} \kappa^2(s,t) \right) ds \tag{30a,b}$$

where according to eqns.(3, 4, 28) the time-dependent tension and bending stiffness of a growing loop in terms of the semiaxes $R_y(t)$ are well-approximated by:

$$\gamma_{o,1/2}(t) = \frac{\pi K}{2} \ln\left(\frac{9R_y(t)}{8r_c} \right); \qquad k_c(t) = \frac{9\pi K R_y^2(t)}{4\sqrt{2}} \tag{31a,b}$$

We note that eqns. (31) used to calculate the total energy E_t are consistent with eqn.(27) since:

$$a(t)=\frac{2\sqrt{2}\ln\left(\frac{9R_y(t)}{8r_c}\right)}{9R_y^2(t)}\approx\frac{4}{R_y^2(t)} \tag{32}$$

Figure 11(a) shows the scaled total energy $E_T/\pi K$ as a function of time (single loop quadrant). The power law is: $E_t = 386t^{0.14}$. The scaled energy increases since S* increases, and also the line tension increases; the term $k_c\kappa^2$ is essentially time-independent.

Figure 11(b) show the ratio of the total tension energy to the total bending energy as a function of time. According to eqns. (30), E_T is a function of S*(t) and the bending energy density which is the product of the bending stiffness times the curvature. Curvature decreases over time, but the bending stiffness increases as a result of increasing in loop size, so this ratio decreases slightly over time, from 1.138 at t=100 s to 1.082 at t=1400 s. At the branch point x_b, the energy ratio is close to 1.

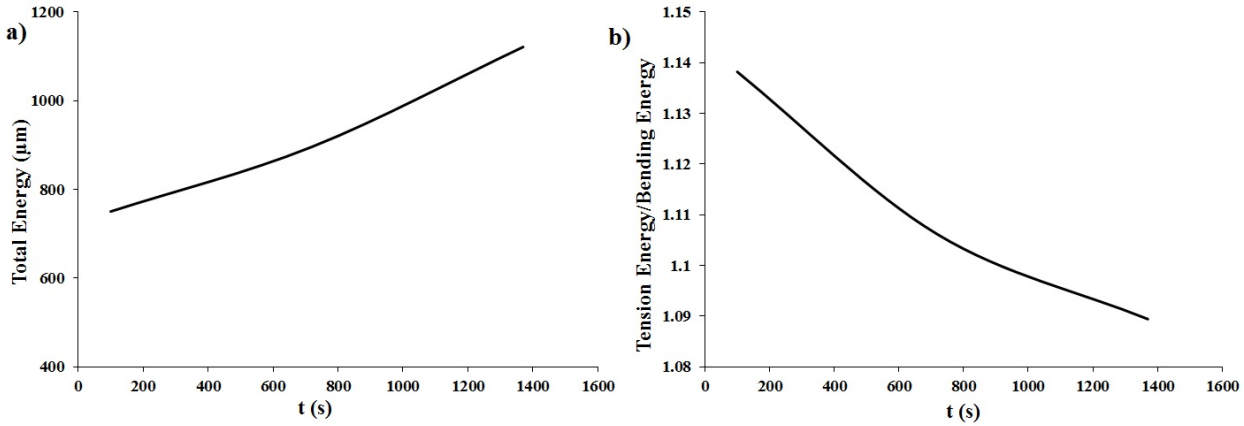

Figure 11. (a) Scaled total disclination line energy $E_T/\pi K$ as a function of time; **(b)** The ratio of the total tension energy per the total bending energy length as a function of t.

Figure 12(a) shows the scaled total energy $E_T/\pi K$ (μm) as a function of the branch point curvature κ^*. Smaller loop radius is accommodated by larger and energetically less costly

curvature. By increasing the loop radius, the branch point curvature κ^* decreases but the scaled total energy $E_T/\pi K$ increases. Figure 12(b) integrates schematically the effects of time on the disclination loop found from simulations (Figs.6-8, 10). In the early stage, small loops lead to high curvature, and low total energy and as time elapses the length S*, tension E_t and bending E_b energies increase while the branch point curvature κ^* and normal velocity ω_n decrease.

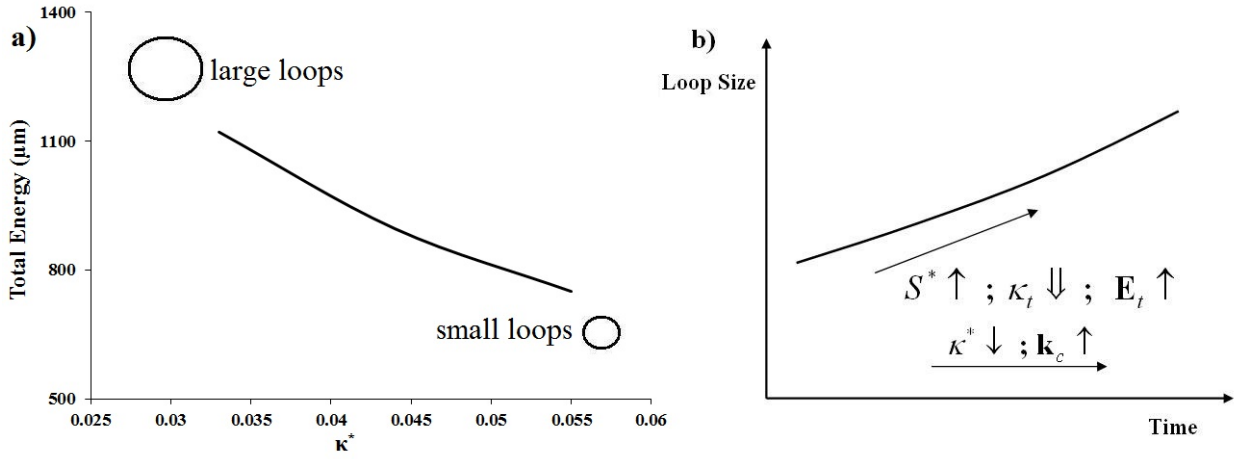

Figure 12. (a) The scaled total energy $E_T/\pi K$ as a function of the branch point curvature κ^*. Increasing the loop size decreases the curvature and increases the total energy; **(b)** Parametric plane indicating the total energy E_T and final arc-length S* of the disclination loop as a function of loop size and time. The loop size increases over time and leads to significant changes in the total energy E_T and final arc-length S*. The growth velocity decreases over time until reaching a terminal velocity.

4. Conclusions

This paper presents theory and simulation of the post nucleation and growth mode of the transformation of a nematic liquid crystal planar radial texture with one axial +1 singular disclination into a planar polar texture with two +1/2 singular disclinations that occurs in a capillary whose surfaces impose homeotropic anchoring. In the initial stages an array of +1/2 loops nucleate on the pre-exiting +1 line and slowly grow by an elastic driving force that is generated by the elimination of the director radial splay. Each +1/2 loop is connected to the +1

line by two branch points and the elliptical cusped loop grows with sub-diffusive kinetics $\left(R_{loop} \approx t^n, n < 1/2\right)$. We presented, solved and characterized a model based on the "nematic elastica" that incorporates tension and bending stiffness. The cusped elliptical loop geometry is the result of strong bending at the two branch points which results in an exponential decrease of curvature when moving away from these cusps. The sub-diffusive loop growth is reflected in the total length, curvature, and dilation. The total energy of the loop increases with decreasing the branch point curvature as the length increase effect is larger than curvature decrease. We demonstrated that when the branch angle is close to $\pi/3$, the material length scale ℓ_M is one half of the loop short axes.

The introduction of a nematic elastica model to solve texture transformations under confinement can in the future be extended to non-planar disclinations where disclination torsion arises. The modeling predictions from the nematic elastica model enhance the current fundamental understanding of defect physics of liquid crystals.

Acknowledgements

This work is supported a grant from the U.S. Office of Basic Energy Sciences, Department of Energy; grant DE-SC0001412.

References

1. M. Kleman and O.D. Lavrentovich, *Soft Matter Physics* (Springer-Verlag, New York, 2003).

2. P. G. de Gennes, *The Physics of Liquid Crystals* (Oxford University Press, New York, 1995).

3. E.G. Virga, *Variational Theories for Liquid Crystals*, (Chapman Hall, London, 1994).

4. I. W. Stewart, *The static and dynamic continuum theory of liquid crystals: a mathematical introduction* (CRC Press, 2004).

5. O. D. Lavrentovich, P. Pasini, C. Zannoni, and S. Zumer, *Defects in Liquid Crystals, Nato Science Series, II. Matehamtics, Physics and Chemsitry*, Vol. 43. (Kluwer Academic Publishers, Netherlands, 2001).

6. G. P. Crawford and S. Zumer, Eds. *Liquid Crystals in Complex Geometries: Formed by Polymer and Porous Networks* (Taylor & Francis, London, 1996).

7. A. Shams, X. Yao, J. O. Park, M. Srinivasarao and A. D. Rey, *Soft Matter*, **8**, 11135-11143 (2012).

8. A. Shams, X. Yao, J. O. Park, M. Srinivasarao and A. D. Rey, MRS Online Proceedings Library, Vol. 1526 (2013); X. Yao, A. D. Rey,J. O. Park and M. Srinivasarao, Lyotropic chromonic liquid crystals in the biphasic region, APS March Meeting Processing, 57(1) (2012).

9. A. Shams, X. Yao, J. O. Park, M. Srinivasarao and A. D. Rey, *Soft Matter,* **10**, 3245−3258 (2014).

10. A. D. Rey, *Soft Matter*, **6(5)**, 3402−3429 (2010); A.D. Rey, *Soft Matter*, **2**, 1349−1368 (2007); A.D. Rey and E. E. Herrera Valencia, *Soft Matter*, **10**, 1611−1620 (2014). B. Wincure and A.D. Rey, *Liquid Crystals*, **34(12)**, 1397−1413, (2007); B. Wincure and A.D. Rey, Nano Letters, **76**, 1474−1479 (2007); B. Wincure and A.D. Rey, Discrete and *Continuous Dynamical Systems, Series B*, **8(3)**, 623−648 (2007); B. Wincure and A.D. Rey, *Continuous Mechanics and Thermodynamics*, **19**, 37−47, 2007; B. Wincure and A.D. Rey, *J. Chem. Phys*., **124**, 244902 (2006).

11. B. T. Gettelfinger, J. A. Moreno-Razo, G. M. Koenig Jr, J. P. Hernández-Ortiz, N. L. Abbott, and J. J. de Pablo, *Soft Matter*, 6(5), 896−901 (2010).

12. M. Srinivasarao, in *Liquid Crystals In The Nineties And Beyond* , S. Kumar editor, 18-19, 377-434 (World Scientific, Singapore, 1995).

13. F. R. Hung, *Phys. Rev. E*, **79(2)**, 021705 (2009).

14- A. D. Rey, *Macromol. Theory Simul.*, **11(9)**, 944-952 (2002).

15- A. Cheong and A. D. Rey, *Phys. Rev. E*, **64**, 041701 (2001).

16- A. D. Rey, *Langmuir*, **19**, 3677−3685 (2003).

17- A. D. Rey, *Soft Matter*, **2**, 1349−1368 (2007).

18- A. D. Rey, *Rheology Reviews 2008*, 71−135 (2009).

19- Y. K. Kim, S. V. Shiyanovskii and O. D. Lavrentovich, *J. Phys.: Condens. Matter*, **25** 404202 (2013).

20. G. De Luca and A. D. Rey, *J. Chem. Phys.*, **126**, 094907 (2007); **127**, 104902 (2007).

21. J. Yan and A. D. Rey, *Phys. Rev. E*, **65**, 031713 (2002); J. Yan and A. D. Rey, *Carbon*, **41**, 105–121 (2003).

22. A. M. Sonnet, E. G. Virga, *Phys. Rev. E*, **56(6)**, 6834−6842 (1997).

23. M. E. Gurtin, *Thermomechanics of Evolving Phase Boundaries in the Plane* (Oxford University Press, New York, 1993).

24. A. D. Rey, *Phys. Rev. E*, **67**, 011706 (2003).

25. A. Ludu, *Nonlinear Waves and Solitons on Contours and Closed Surfaces* (Springer-Verlag: Berlin, 2007).

26. N. M. Neil, *Phys. Rev. E*, **68**, 036305 (2003).

27. W. Kuhnel and B. Hunt, *Differential Geometry: Curves - Surfaces - Manifolds* (American Mathematical Society: US, 2006).

28. Yu. A. Nastishin, K. Neupane, A. R. Baldwin, O. D. Lavrentovich, and S. Sprunt, *electronic-Liquid Crystal Communications,* July 18, 1−4 (2008).

Appendix I

Numerical Methods

To find the evolving loop shape y(x,t) we solve equations (8, 10 and 11) using time-dependent boundary conditions subjected to constraints given by eqn.(12). The computational domain is discretized into n=100 nodes. To find the final curvature (κ^*) and initial values for the bending to tension ratio (a) we use the following initial guess as per our previous work [7]:

$$\kappa^* = 10/3y^*(t),\ a=\left(3/y^*(t)\right)^2 \qquad \text{(A1)}$$

The boundary conditions are:

$$y(1)=y^*(t);\ x(1)=0;\ \kappa(1)=0$$
$$y(n)=0;\ x(n)=x_b(t);\ \kappa(n)=\kappa^* \qquad \text{(A2a,b)}$$

From our previous work [7-9] the analytical solution for the shape equation (8) is given by:

$$\kappa = \pm 2\sqrt{a}\left\{\frac{-2Ce^{-\sqrt{a}s}}{\left(C^2\left(e^{-\sqrt{a}s}\right)^2+1\right)}\right\}; C = \frac{\sqrt{4a-\kappa_o^{\,2}}-\sqrt{4a}}{\kappa_o} \tag{A3}$$

where $\kappa(s=0,t)=\kappa_o$. To find the arc-length at the i[th] node we use eqn.(A3):

$$s(i) = 2\sqrt{a}\ln\left(\frac{1}{C-\kappa(i)-\frac{2\sqrt{a}}{\kappa(i)}}\right) \tag{A4}$$

in a loop for i≥2. Then we find x(i) and y(i) :

$$\mathrm{x(i)} = \int_{\mathrm{s(1)}}^{\mathrm{s(i)}} \cos(\theta)\mathrm{ds} + \mathrm{x(1)} \tag{A5}$$

$$\mathrm{y(i)} = \int_{\mathrm{s(1)}}^{\mathrm{s(i)}} \sin(\theta)\mathrm{ds} + \mathrm{y(1)} \tag{A6}$$

where φ is tangent angle defined as follow

$$\varphi(i) = \alpha + \frac{\pi}{2} + \int_{s(n)}^{s(i)} \kappa(i)ds \tag{A7}$$

The value of s(n) is found from:

$$at\ \ s = s^*: \int_{s(n)}^{0} \kappa(i)ds = \frac{\pi}{3} - \frac{\pi}{2} \tag{A8}$$

The slope dy/dx at the branch point must satisfy:

$$dy/dx\,(at\ \mathrm{s=S^*}):\tan(60^\circ);\ y(n) = \left[x(n)-x(n-1)\right]\tan(60^\circ) + y(n-1) \tag{A9}$$

If the branch angle is essentially equal to 60° (error<0.01), the initial guess for κ^* and a is acceptable, otherwise we redo the loop calculation. After each converged step, time is up-dated in the forward-marching scheme:

$$t = t + h \tag{A10}$$

where h is the time step.

Appendix II

In this appendix we establish the origin of the branch point angle φ_o,= 60° shown in Figure 4. As the loop grows, both tension and bending stiffness change, as indicated in eqns.(27, 31). The ratio $a = \gamma_{0,1/2}/k_c$ decreases with increasing R_y and hence the bending stiffness increases (eqn.(32)). As the material parameter $a = \gamma_{0,1/2}/k_c$ evolves , the geometry also evolves , increasing the total loop length and decreasing the total loop curvature. The imposed constant branch angle is the condition that leads to the balance between these two effects.

Figure A1 shows the branch point angle as a function of the loop radius R_y, for several values of $a = \gamma_{0,1/2}/k_c$. The lines cross the 60° branch angle value at Ry values that satisfy equation (32). We conclude that the 60° branch angle constraint simply indicates that the material length scale is one half of the geometric scale R_y: $1/\sqrt{a(t)} \approx R_y(t)/2$. This length increases over time as shown in figure A2. This last figure also shows that the inverse of the curvature at the branch point $1/\kappa^*$. Scales linearly with Ry. Figure A2 demonstrates that the branch angle φ_o,= 60° is due to the consistency of the three length scales: Ry, $1/\kappa^*$.and l_M.

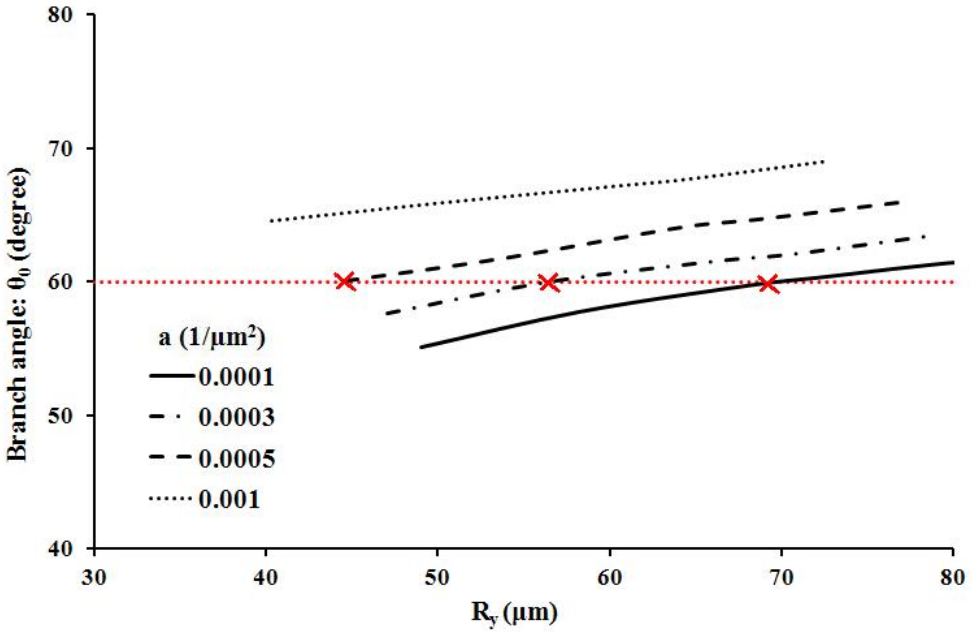

Figure A1. Branch point angle as a function of the loop short radius under capillary confinement, computed using a fixed the tension/bending stiffness ratio $a = \gamma_{0,1/2}/k_c$ and changing the final curvature κ^*.

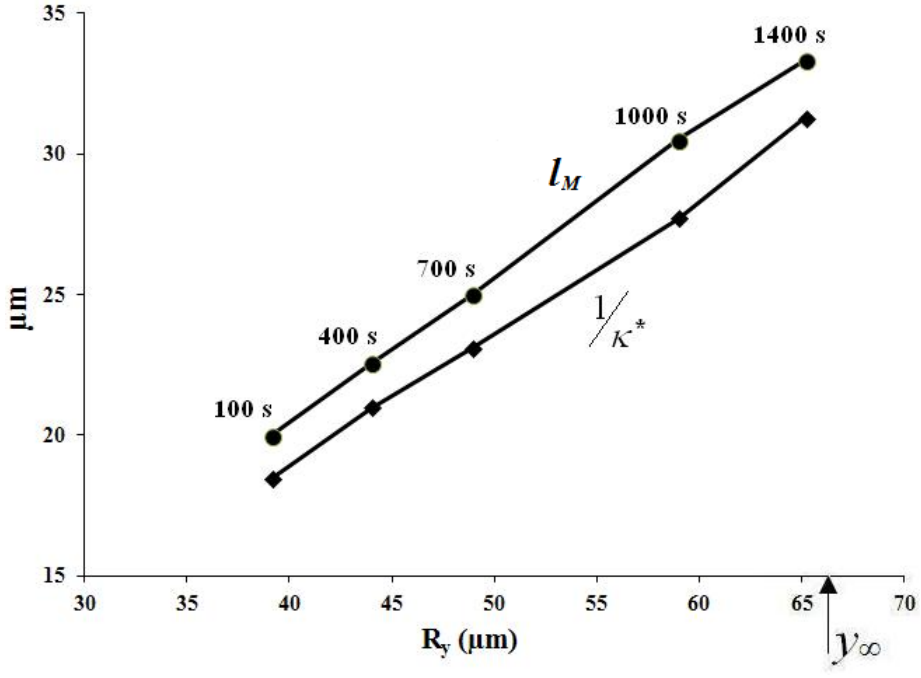

Figure A2. Material length scale, l_M, and the reverse of the branch point curvature as a function of R_y for different time. The two length scales are linear functions of Ry and of the same order of magnitude.

Appendix III

The purpose of Appendix III is to demonstrate that line viscous dissipation is negligible. The line viscosity is:

$$\mu = \pi r_c^2 \gamma_1 \tag{A11}$$

where γ_1 is the rotational viscosity and r_c the defect core radius. Next we compare the line tension force $\gamma_{0,1/2}\kappa$ with the viscous force $\mu\partial\kappa/\partial t$. The values of the line tension and rotational viscosity can be estimated by studying the uniform motion of the branch points. The branch point velocity can be estimated from the dR_x/dt. Assuming that the Frank elastic constant is K≈10 pN, which is a measured value for a well-studied chromonic LC-DSCG by dynamic light scattering [28], we estimate that the rotational viscosity is $\gamma_1 \approx$ 5 Pa.s. According to equation 4(b), the bending modulus is $k_c \approx 2.5\text{x}10^{-7}$ pN.m^2 and using Figure (A1), the bare line tension is estimated $\gamma_0 \approx 200$ pN. Figure A3 shows the ratio of the line tension force ($\gamma_{0,1/2}\kappa$) to the viscous force $\mu\partial\kappa/\partial t$ as a function of time. It can be seen even for small loops the viscous term is negligible.

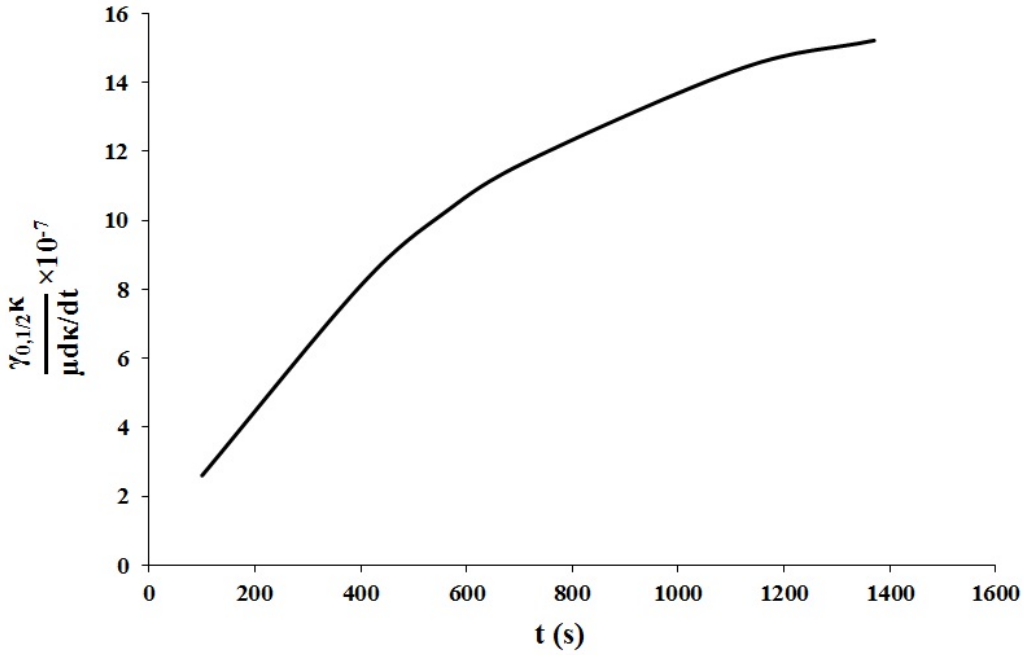

Figure A3. The ratio of tension forces to the viscose force. It can be seen the viscous force is negligible compared to the line tension force.